Backscattering X-ray standing waves in the XUV region

T. M. Grehk,[a]† W. Drube,[a]* L. Kipp[b] and G. Materlik[a]

[a]Hamburger Synchrotronstrahlungslabor HASYLAB am Deutschen Elektronen-Synchrotron DESY, Notkestrasse 85, 22603 Hamburg, Germany, and [b]Institut für Experimentelle und Angewandte Physik, Leibnizstrasse 19, 24098 Kiel, Germany. E-mail: wolfgang.drube@desy.de

It is demonstrated that Bragg reflection of XUV radiation can be used to study structural properties of crystalline materials with large unit cells. A standing-wave field is formed in a layered $TiSe_2$ single crystal for a near-backscattering geometry ($\Theta = 88.5^\circ$). The partial electron yield is measured as a function of photon energy across the (001) Bragg reflection condition ($h\nu \simeq 1033$ eV) and its characteristic modulation is compared with the results derived from dynamical diffraction theory in the two-wave approximation. The data reveal a large amount of disorder along the *c*-axis.

Keywords: X-ray standing waves; XUV Bragg reflection; normal-incidence dynamical diffraction; $TiSe_2$.

1. Introduction

X-ray standing waves (XSW) are a well established tool for determining the local geometry of adsorbates on single-crystal surfaces, the structure of buried interfaces and the site of impurity atoms (Bedzyk *et al.*, 1989; Zegenhagen, 1993; Cowan *et al.*, 1980; Materlik *et al.*, 1985; Woodruff *et al.*, 1987; Sugiyama *et al.*, 1995). This method monitors secondary emission yields from atoms, such as fluorescence radiation or photoelectrons and Auger electrons, as a function of the position of the standing X-ray wave field relative to the diffracting planes of a crystalline sample. The phase variation is controlled by either sweeping the incidence angle or the photon energy through the corresponding Bragg reflection.

For almost perfect single crystals, XSW can be applied over a large range of incidence angles using conventional X-ray energies. Since these energies are typically around 10 keV, samples can be studied under ambient conditions. In such a case there are high demands on angular collimation and/or energy resolution of the exciting beam since the dynamical Bragg reflection properties of the crystal under investigation have to be matched. For crystals which are usually less perfect, such as for many metals, it is advantageous to choose a longer wavelength in order to reach Bragg angles close to 90° where the Bragg reflection becomes less sensitive to angle variations. Near normal incidence, *i.e.* backreflection, the lattice constant directly determines the Bragg wavelength, $\lambda \simeq 2d$, which requires a considerably lower photon energy, in the range of a few keV. Therefore, these studies are commonly performed *in vacuo* using standard surface-science equipment. Besides the possibility to study non-perfect samples, the lower photon energies permit the study of low-*Z* elements with high sensitivity and make use of the larger photoelectric cross sections which in turn allows the use of photoelectron or Auger electron secondary yields more effectively. In backreflection XSW measurements the Bragg condition is commonly tuned by varying the photon energy instead of the incidence angle. There are more XSW means to study structural properties of materials with large *d*-spacing, such as total external Fresnel reflection for mirror surfaces (Bedzyk *et al.*, 1989) and Langmuir–Blodgett multilayers (Iida *et al.*, 1985). Both methods, however, are normally also used with photon energies of around 10 keV.

It is thus interesting to investigate the applicability of XSW at even longer wavelengths in order to explore the possibilities of utilizing low-order reflections from crystals with larger unit cells. Examples of such materials are the $Cu_{1-x}O_x$-based superconductors, SiC poly types and layered structures such as the transition-metal dichalcogenides (TMDC). For our study we chose 1T-$TiSe_2$ which is a prototype TMDC compound. The macroscopic and microscopic properties of these layered crystals show a pronounced two-dimensional character. While inside one layer the strong ionic and covalent bonding predominates, weak van der Waals forces act between the layers. Consequently, the TMDCs exhibit strong anisotropic properties (*e.g.* in optical and electronic properties).

Inside one layer the transition-metal atom Ti is hexagonally surrounded by six other Ti atoms. This plane of metal atoms is sandwiched by two layer planes of hexagonal-close-packed Se atoms. The chalcogen atoms are coordinated octahedrally with regard to the transition-metal atom. Different stacking sequences of the layers result in the polymorphic types of the crystals with different lattice parameters *c* perpendicular to the layers. $TiSe_2$ crystallizes in the 1T structure, *i.e.* one sandwich contributes to *c*. Single crystals can be grown with reasonable perfection and size by an iodine gas transport reaction.

The weak interaction between layers also allows intercalation of additional atoms or molecules which may drastically change the interlayer distances and the electronic properties (Wu *et al.*, 1996). The XSW technique, applied to such a system, would be a powerful tool for the determination of lattice and dopand distances.

The general relation between photon wavelength and Bragg angle, as given by Bragg's law, can be visualized using a DuMond plot (DuMond, 1937). Here we consider the special case of a Bragg condition for $TiSe_2(001)$ around $\Theta = 90^\circ$. Fig. 1 shows a calculated contour plot for the corresponding photon energy *versus* angle relation close to normal incidence, *i.e.* backreflection. The contour data are obtained from the dynamical theory of X-ray diffraction (see below) for the symmetric Bragg case, *i.e.* the diffraction planes are parallel to the surface. As indicated in the figure, a crystal reflection curve can be measured by either scanning the angle or by tuning the photon energy. However, owing to the strong non-linearity close to $\Theta = 90^\circ$, drastically different reflection curves are obtained. At $\Theta = 90^\circ$ the energy dispersion as a function of angle vanishes and as a consequence the energy width of the reflection curve, taken as the full-width-at-half-maximum (FWHM) value of its intensity, goes through a minimum in this range. The angular reflection curve, on the other hand, becomes much broader. This is shown in Fig. 2 where angle scans (at $h\nu = 1032.9$ eV) and energy scans (at $\Theta = 88.5^\circ$) are compared. While the angle scan is broad and highly asymmetric with a tail to higher angles, the energy scan is symmetric and narrow.

In order to model the measured reflection curves, the finite energy resolution of the monochromator and the angle divergence in both the horizontal and vertical direction has to be taken into account. In most cases, only one divergence contributes significantly to the spectral broadening. The angle divergence of a grating monochromator is mainly determined by the setting of the horizontal and vertical slit systems and can therefore be considered as fixed over a large energy interval. The energy resolution, on the other hand, depends on many factors, but it is often reasonable to assume that over small energy intervals both the energy and angle resolution of a

† Present address: Högskolan Dalarna, 781 88 Borlänge, Sweden.

grating monochromator are constant, as indicated by the ellipsoid in Fig. 1.

In this study it is demonstrated that X-ray standing waves can be utilized even in the XUV range using grating monochromators. We also derive a new expression for the Bragg reflectivity and partial yield signal in the two-wave approximation for the symmetric Bragg case, which is valid at all Bragg angles and does not apply the commonly used approximations. Layered $TiSe_2$ single crystals were investigated in backscattering geometry. The results indicate considerable disorder along the probed (001) crystal direction and show that XSW can be effectively used to obtain structural information for crystals with large unit cells.

2. Experimental details

The experiments were performed at the XUV-undulator beamline BW3 at HASYLAB, Hamburg (Larsson *et al.*, 1994). The optical path comprises a plane-grating SX-700 monochromator, a pre-mirror and a refocusing mirror. While in our experiment the vertical beam divergence can be neglected, the contribution of the horizontal fan has to be considered quantitatively in the analysis. As an approximation, we assume a Gaussian-like distribution with a half width given by the acceptance angle of the refocusing mirror and the demagnification ratio. In our case this amounts to ~4 mrad. The photon energy resolution, as determined by the slit settings of the grating monochromator, was set to 0.4 eV. At the experimental station, photoelectrons from the sample were measured by a hemispherical electron energy analyzer (SCIENTA SES 200). Electron energy distribution curves (EDC) were recorded with an energy resolution of 0.3 eV. This is essential in order to precisely calibrate and tune the Bragg angle, which is accomplished by rotating the sample relative to the incoming beam near normal incidence. The samples were mounted on a high-precision manipulator which can be accurately positioned by stepping motors.

Before hitting the sample, the primary beam passes through the centre bore of an electrically isolated metal plate. For Bragg angles slightly below 90°, this plate blocks the reflected beam from the sample and thus serves as a reflectivity monitor by measuring its photoelectron drain current. In order to decrease the contribution of secondary electrons from the sample to the net current signal, this monitor was biased by a potential of −300 V. Since the geometry of the monitor and its aperture was known, the manipulator settings could be accurately calibrated by an iterative change of the sample angles combined with photon energy scans while observing the monitor signal.

Single crystals of $TiSe_2$ were grown by chemical vapour transport using iodine as transport agent. The crystals grew as thin platelets with a surface area up to 5 mm^2. For the experiment they were carefully glued onto a flat sample holder surface. Also, we only selected samples with a minimum thickness of 0.5 mm in order to avoid crystal deformation during hardening of the expoxy glue. Clean sample surfaces were obtained by cleavage *in vacuo* by ripping off a stainless level arm glued on top of the sample. The resulting surfaces were optically flat and shiny. The surface quality was investigated by photoemission and LEED, which showed sharp (1 × 1) spots and negligible background across the entire surface.

Partial electron yield data were obtained in a constant final-state mode for Ti (Ti L_2–$M_{2,3}M_{2,3}$ Auger transition) and in a constant initial-state mode for Se (Se 3*p*). For these scans the electron energy resolution was set to 0.6 eV. The total accumulation time per scan was less than 15 min.

3. Theory

In the analysis, we follow the theoretical treatment of dynamical diffraction of X-rays by perfect crystals described by Graeff & Materlik (1982). The wave field in the crystal is written as the sum of plane waves satisfying Maxwell's equations for a three-dimensional

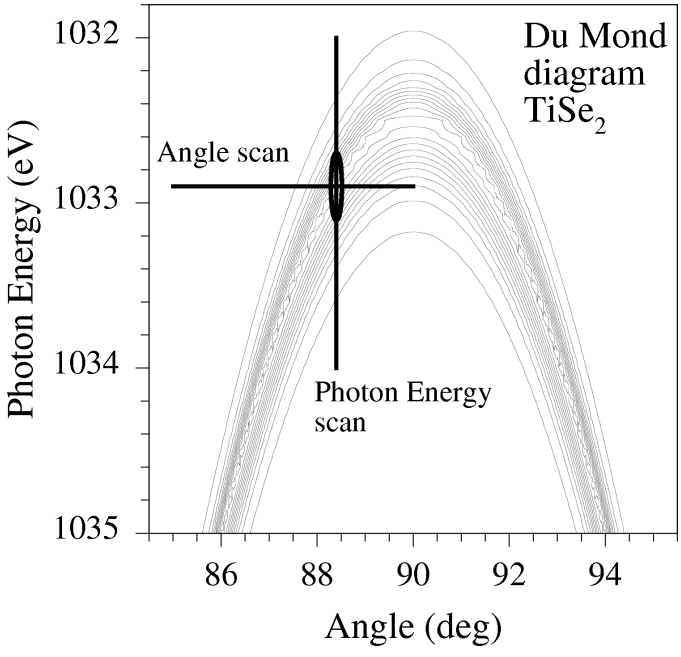

Figure 1
DuMond diagram for $TiSe_2$ close to $\Theta_B = 90°$. The contour plot was calculated using the values in Table 1. The horizontal line marks an angle scan and the vertical line marks an energy scan. The resolution function of the grating monochromator is indicated as an ellipsoid.

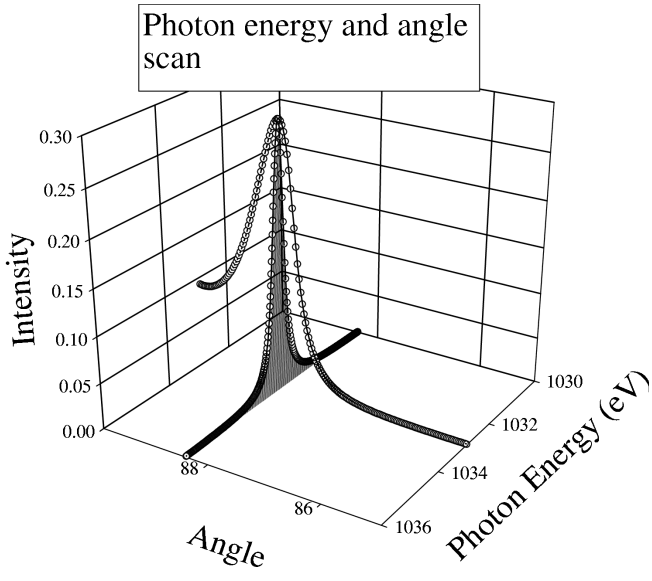

Figure 2
Three-dimensional plot showing the different reflectivity curves obtained by an angle scan at 1032.9 eV and photon energy scan at 88.5° (*cf.* Fig. 1).

periodic potential lattice. The resulting set of equations can be significantly simplified for the case where only one point in reciprocal space is near the Ewald sphere and generates a diffracted beam. Then, only two waves have to be considered, the incoming beam $\mathbf{E}_0$ and the diffracted beam $\mathbf{E}_H$ (two-wave approximation). The allowed wave vectors are obtained by solving a set of two secular equations which contain fourth-order terms of the wave vectors. Usually the analysis is restricted to Bragg angles sufficiently below 90° to implement an approximation which reduces the order of the secular equation. Clearly, such derived results for the field amplitudes as a function of incidence angle, $\mathbf{E}_0(\Theta)$ and $\mathbf{E}_H(\Theta)$, are not applicable in the case of backreflection. It is, however, possible to give a solution in photon energy space using the differential form of the Bragg equation (Woodruff *et al.*, 1988). Then, $\mathbf{E}_0(h\nu)$, $\mathbf{E}_H(h\nu)$ is valid also for $\Theta_B = 90°$.

Here we chose to solve the fourth-order equation analytically without further approximation (Zegenhagen *et al.*, 1990; Graeff & Materlik, 1982; Brümmer *et al.*, 1979; Caticha & Caticha-Ellis, 1982).

The initial set of equations is

$$\begin{vmatrix} \mathbf{k}^2(1-\chi_0) - \mathbf{K}_0^2 & -\chi_{\overline{H}}\mathbf{k}^2 P \\ -\chi_H \mathbf{k}^2 P & \mathbf{k}^2(1-\chi_0) - \mathbf{K}_H^2 \end{vmatrix} = 0, \quad (1)$$

where $\mathbf{K}_0$ and $\mathbf{K}_H$ are the wave vectors of the incoming and reflected wave inside the crystal, $\mathbf{k} = \nu/c$ is the wavevector and P is the polarization factor of the incoming beam outside the crystal. The quantities χ_0, χ_H and $\chi_{\overline{H}}$ are the Fourier components of the electric susceptibility defined as

$$\chi_H = r_e \lambda^2 F_{[h,k,l]}/\pi V, \quad (2)$$

where λ is the wavelength of the light, r_e is the classical electron radius, $F_{[h,k,l]}$ is the complex scattering amplitude and V is the volume of the unit cell. The $F_{[h,k,l]}$ values were obtained using the program code of Brennan & Cowan (1992).

Assuming that the lattice planes are parallel to the surface, we obtain, for the ratio between the incoming and reflected wave amplitudes,

$$\mathbf{E}_H/\mathbf{E}_0 = \left(\chi_H/\chi_{\overline{H}}\right)^{1/2}\left[\eta \pm \left(\eta^2 - 1\right)^{1/2}\right], \quad (3)$$

with

$$\eta = \frac{\left[(g/k)^2\left(\sin^2\Theta - \chi_0\right) + \chi_{\overline{H}}\chi_H P^2\right]^{1/2} - (1/2)(g/k)^2}{\left(\chi_{\overline{H}}\chi_H\right)^{1/2} P}, \quad (4)$$

where g is the magnitude of the reciprocal lattice vector. Equation (3) is formally equivalent to the result derived by Batterman & Cole (1964); however, the angular variable η is now valid at all angles (see Appendix *A*).

The reflectivity $R(h\nu, \Theta)$ is obtained as

$$R(h\nu, \Theta) = \left|\mathbf{E}_H/\mathbf{E}_0\right|^2, \quad (5)$$

and for the partial yield, $Y(h\nu, \Theta, f, p)$, one has

$$Y(h\nu, \Theta, f, p) = 1 + R(h\nu, \Theta) + 2f\left[R(h\nu, \Theta)\right]^{1/2} \times \cos[\varphi(h\nu, \Theta) - 2\pi p], \quad (6)$$

where f is the coherent fraction, *i.e.* the fraction of atoms at the coherent position, p, relative to the lattice planes. Since the reflectivity R depends on the photon energy and the incidence angle, the monochromator energy distribution and the divergence of the incident beam both have to be considered quantitatively in order to compare the calculated data with the experiment. As an approximation, we assumed a Gaussian distribution in both cases.

4. Result and discussion

The $TiSe_2$ crystals have a 1T-CdI_2 structure where, within the layer, Ti is covalently bonded to two Se atoms at the positions $(\frac{1}{3}, \frac{2}{3}, z)$ and $(\frac{2}{3}, \frac{1}{3}, -z)$ where $z = 0.25504$ in units of the lattice constant (Riekel, 1976). In the (001) direction the unit cell has a length of 6.008 Å. The bonds between adjacent $TiSe_2$ sandwiches are van der Waals-type interactions and they are correspondingly weak. The layered structure of the material results in a high anisotropy of the physical properties. From the lattice constant a Bragg energy of 1032.9 eV is calculated at normal incidence. In our experiment we chose an incidence angle of 88.5°, which is compatible with the geometry of the reflection monitor.

Core-level spectra of Se (3*d*) and Ti (3*p*) recorded around the nominal Bragg energy (1032.9 eV) are shown in Fig. 3. Both peaks exhibit appreciable intensity modulation as the photon energy is tuned through the Bragg condition. For the off-Bragg energies, *i.e.* at 1030 eV and 1036 eV, the corresponding EDCs have similar intensities for both elements, respectively. The modulation of the Se 3*d* yield follows the development of the reflection curve (Fig. 4) with a maximum at 1032.9 eV, whereas the Ti 3*p* line shows a completely different behaviour with a minimum just below (1032.4 eV) the reflection maximum and a maximum just above (1033.4 eV). The Ti signal mimics the behaviour of the corresponding total electron yield

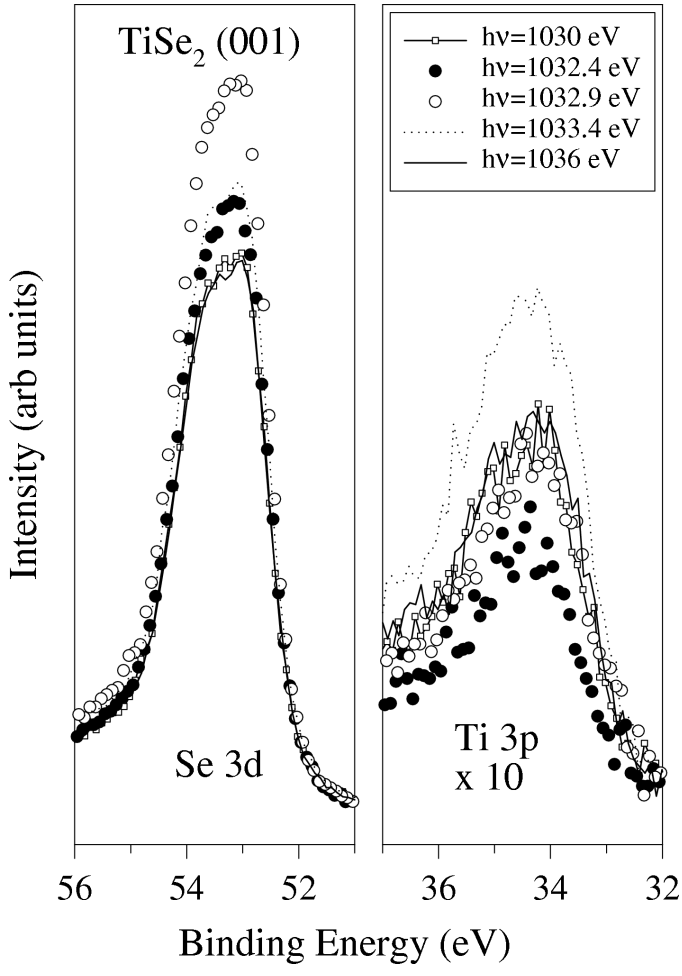

Figure 3
Se 3*d* and Ti 3*p* electron energy distribution curves recorded for photon energies around the Bragg reflection.

Table 1
Input parameters used in the calculation of the $TiSe_2$ reflection and partial yield curves.

Quantity	Value
c	6.008×10^{-10} m
$F'_{0,0,0}$	71.89
$F''_{0,0,0}$	$13.78i$
$F'_{0,0,0,1} = F'_{0,0,0,-1}$	17.89
$F''_{0,0,0,1} = F''_{0,0,0,-1}$	$5.87i$
V	6.5203×10^{-29} m^3

signal, displayed in Fig. 5, although the relative amplitudes differ. This arises because the electron density determines the position of the XSW nodes inside the crystal. The two Se atoms have a larger number of electrons than Ti but the centre of the elastically scattering charge density with (001) periodicity is at the Ti site. As a consequence, the yield corresponding to a coherent position of $p = 0$ [0 is equivalent to 1; *cf.* equation (6)] dominates the total yield.

The measured and calculated values for the reflection curve and the partial yields from Se and Ti are shown in Fig. 4 and Fig. 6, respectively. The input parameters for the calculations are given in Table 1. The width of the measured reflection curve (0.8 eV) is somewhat larger than the calculated value (0.7 eV) and the line profile exhibits an asymmetry towards lower photon energies. We attribute this asymmetry to an experimental artefact caused by high-energy electrons from the sample which contribute to the total yield signal of the reflection monitor. In a later design of this device, this potential problem was minimized by additional electrically biased guard meshes in front of the monitor. The contribution of stray electrons, however, cannot explain the slightly larger width of the measured reflection curve. We attribute part of the broadening to disorder in the sample along the probed crystal direction.

The fit of the partial yield curves (Fig. 6) only left the coherent fraction as a free parameter. For Ti the best result was obtained for $f = 0.5$ instead of for $f = 1.0$. This again indicates a substantial crystal

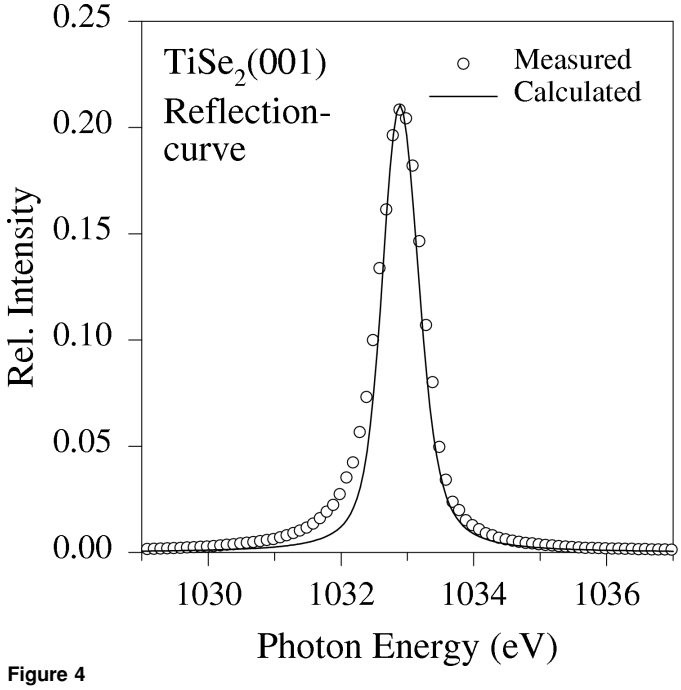

Figure 4
Measured and calculated $TiSe_2$ (001) reflection curves. The measured data are the photoelectron yield signal from the reflection monitor.

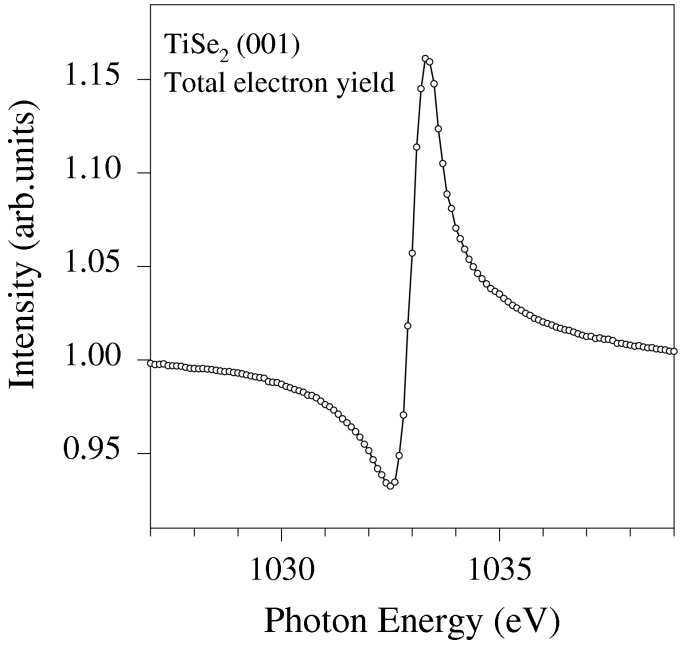

Figure 5
The total-electron-yield signal (sample drain current) around the Bragg photon energy. The incidence is fixed at 88.5°.

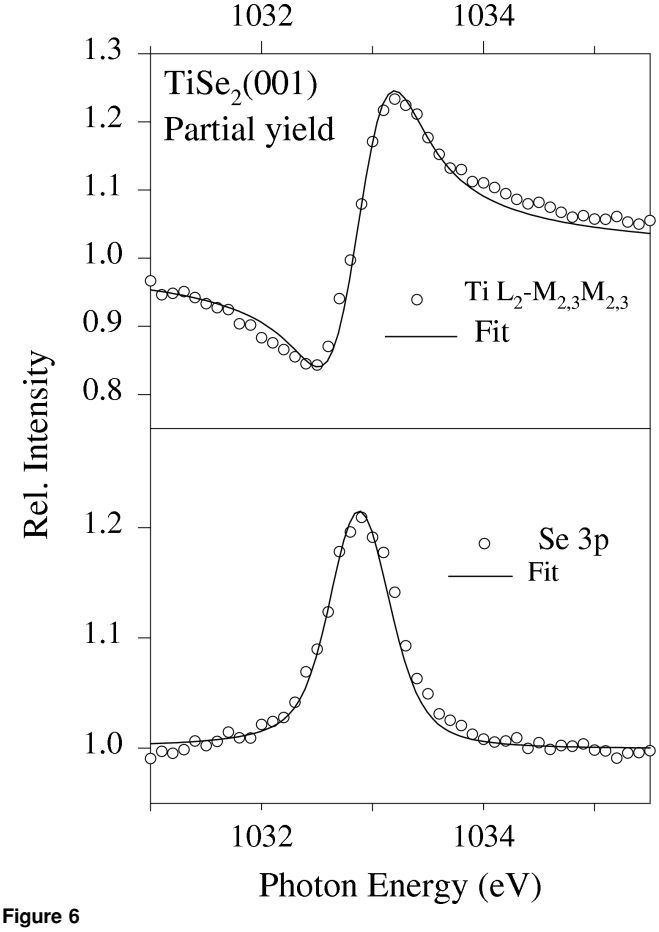

Figure 6
Measured and calculated partial yield curves obtained for Ti and Se. The Ti signal was recorded in a constant final-state mode and the Se signal was recorded in a constant initial state measurement.

disorder along the *c* direction. The high-quality LEED images, on the other hand, supported a high lateral order. In a recent combined scanning tunnelling microscopy and photoemission study of Na intercalation in the layered VSe_2 system (Brauer *et al.*, 1997), a model was proposed where the intercalating atoms grow in two-dimensional islands. Such a model would also be compatible with our findings, since two-dimensional islands formed by intercalating atoms would have a lateral order similar to the undisturbed areas but induce a modulation along *c*. It is thus reasonable to interpret the reduced coherent fraction as an indicator for intercalation-induced disorder which may be caused by the incorporation of excess Ti atoms during crystal growth.

The Se partial yield resembles the shape of the reflection curve. This occurs because two different Se sites, $c = 0.255$ and $c = -0.255$, contribute to the signal. The calculated individual partial yield curves are shown in Fig. 7 for coherent fractions ranging from 1 to 0.5. The sum of the yield curves corresponding to the different sites (top panel in Fig. 7) appears to be almost independent of the coherent fraction. The Se signal is of course sensitive to the scattering factors (keeping the other parameters fixed), and the fit between the measured data and the calculation can be utilized to test the validity of these data. The good agreement between measured and calculated partial yields for Se gives a satisfactory support for the scattering factors used in the calculations.

5. Conclusions

We have shown that X-ray standing waves can be generated even at appreciably low energies around 1000 eV. We used the (001) reflection from a layered $TiSe_2$ crystal and measured the modulation of the Se and Ti electron yield as a function of photon energy in a backscattering geometry. The data indicate substantial disorder along the (001) direction, *i.e.* normal to the layers. XSW at these longer wavelengths thus provide a precise tool for studying structural properties of large unit-cell materials together with their electronic properties.

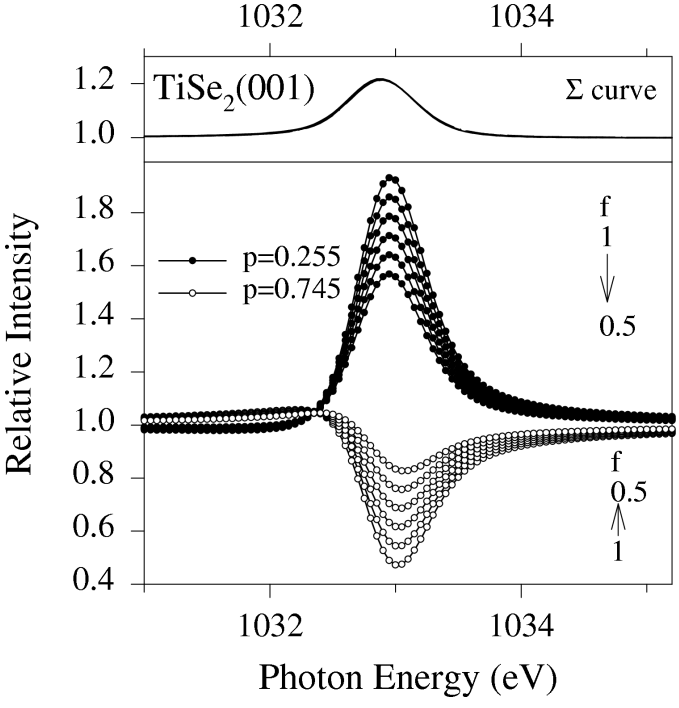

Figure 7
Partial yield curves calculated for Se with different coherent fractions. Because the Se positions are close to $z = 0.25$ and $z = -0.25$, the sum of the individual yields (Σ) is independent of the coherent fraction.

APPENDIX *A*
Derivation of equation (4)

In the two-wave approximation, Maxwell's equations can be written as

$$\begin{aligned}&\left[\mathbf{k}^2(1-\chi_0)-\mathbf{K}_0^2\right]\mathbf{E}_0-\chi_{\overline{H}}\mathbf{k}^2P\,\mathbf{E}_H=0\\&-\chi_H\mathbf{k}^2P\,\mathbf{E}_0+\left[\mathbf{k}^2(1-\chi_0)-\mathbf{K}_H^2\right]\mathbf{E}_H=0,\end{aligned}\tag{7}$$

where $\mathbf{k}$ is the wavevector outside the crystal and $\mathbf{K}_0$ and $\mathbf{K}_H$ are the incoming and reflected wave vectors inside the crystal. χ_0, χ_H and $\chi_{\overline{H}}$ are the matrix elements of the electric susceptibility defined as

$$\chi_H = r_e\lambda^2F_{[h,k,l]}/\pi V.\tag{8}$$

From (7) it follows that

$$\frac{\mathbf{E}_H}{\mathbf{E}_0}=\frac{\mathbf{k}^2(1-\chi_0)-\mathbf{K}_0^2}{\chi_{\overline{H}}\mathbf{k}^2P}=\frac{\chi_H\mathbf{k}^2P}{\mathbf{k}^2(1-\chi_0)-\mathbf{K}_H^2}.\tag{9}$$

To solve (7) one has

$$\begin{vmatrix}\mathbf{k}^2(1-\chi_0)-\mathbf{K}_0^2 & -\chi_{\overline{H}}\mathbf{k}^2P\\ -\chi_H\mathbf{k}^2P & \mathbf{k}^2(1-\chi_0)-\mathbf{K}_H^2\end{vmatrix}=0,\tag{10}$$

yielding

$$\left[\mathbf{k}^2(1-\chi_0)-\mathbf{K}_0^2\right]\left[\mathbf{k}^2(1-\chi_0)-\mathbf{K}_H^2\right]-\chi_{\overline{H}}\chi_H\mathbf{k}^4P^2=0.\tag{11}$$

Following the path sketched by Graeff & Materlik (1982), the coordinates are changed as shown in Fig. 8,

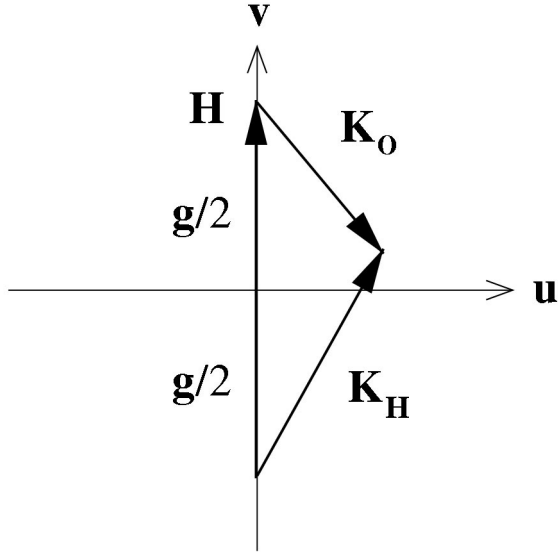

Figure 8
Change of coordinates from (**K**, **H**) to (**v**, **u**) where **g** denotes the reciprocal lattice vector.

$$\mathbf{K}_0 = \mathbf{u} - [(\mathbf{g}/2) - \mathbf{v}]$$
$$\mathbf{K}_H = \mathbf{u} + [(\mathbf{g}/2) + \mathbf{v}]. \quad (12)$$

Using the short-hand notations

$$\Omega = \chi_{\overline{H}}\chi_H \mathbf{k}^4 P^2,$$
$$\beta = \mathbf{k}^2(1 - \chi_0), \quad (13)$$

equations (11)–(13) yield

$$\beta^2 - \beta(\mathbf{K}_0^2 + \mathbf{K}_H^2) + \mathbf{K}_0^2\mathbf{K}_H^2 - \Omega = 0,$$

$$\mathbf{v}^4 + \mathbf{v}^2(2\mathbf{u}^2 - 2\beta - \mathbf{g}^2/2) + \mathbf{u}^4 + \mathbf{u}^2(\mathbf{g}^2/2 - 2\beta) + \mathbf{g}^4/16 - \beta\mathbf{g}^2/2 + \beta^2 - \Omega = 0.$$

Solving for $\mathbf{v}^2$,

$$\mathbf{v}^2 = \left[\beta + \left(\mathbf{g}^2/4\right) - \mathbf{u}^2\right] \pm \left(\beta\mathbf{g}^2 + \Omega - \mathbf{u}^2\mathbf{g}^2\right)^{1/2}. \quad (14)$$

Since $\mathbf{g}/2 \simeq \mathbf{k}$, the plus sign yields a non-physical solution. With the new coordinates, equation (9) reads,

$$\frac{\mathbf{E}_H}{\mathbf{E}_0} = \left[\mathbf{k}^2(1 - \chi_0) - \mathbf{K}_0^2\right]/\left(\chi_{\overline{H}}\mathbf{k}^2 P\right)$$
$$= \left\{\beta - \mathbf{u}^2 - [(\mathbf{g}/2) - \mathbf{v}]^2\right\}/\left(\chi_{\overline{H}}\mathbf{k}^2 P\right)$$
$$= \left(\chi_H/\chi_{\overline{H}}\right)^{1/2} \frac{\left[\mathbf{gv} - (\mathbf{g}^2/2) + (\beta\mathbf{g}^2 + \Omega - \mathbf{u}^2\mathbf{g}^2)^{1/2}\right]}{\left(\chi_{\overline{H}}\chi_H\right)^{1/2}\mathbf{k}^2 P}. \quad (15)$$

In the following, it is assumed that the lattice planes are parallel to the crystal surface. Since the component of the electric field parallel to the surface is conserved,

$$u = \mathbf{k} \cdot \mathbf{n}_e = k \cos\Theta, \quad (16)$$

where $\mathbf{n}_e$ is the surface normal and Θ denotes the Bragg angle. Defining

$$y^2 = 1 - \chi_0 - \cos^2\Theta + \Omega/(k^2 g^2),$$

equation (14) then yields

$$\mathbf{v}^2 = k^2\left[1 - \chi_0 + \left(g^2/4k^2\right) - \cos^2\Theta\right] - kg\left[1 - \chi_0 - \cos^2\Theta + \Omega/(k^2 g^2)\right]^{1/2}$$
$$= (ky - g/2)^2 - \Omega/g^2, \quad (17)$$

and consequently from (15)

$$\frac{\mathbf{E}_H}{\mathbf{E}_0} = \left(\frac{\chi_H}{\chi_{\overline{H}}}\right)^{1/2} \frac{\left\{gky - (g^2/2) \pm g\left[(ky - g/2)^2 - \Omega/g^2\right]^{1/2}\right\}}{\left(\chi_{\overline{H}}\chi_H\right)^{1/2}k^2 P}$$
$$= \left(\frac{\chi_H}{\chi_{\overline{H}}}\right)^{1/2}\left[\eta \pm \left(\eta^2 - 1\right)^{1/2}\right], \quad (18)$$

where

$$\eta = g(ky - g/2)/\left(\chi_{\overline{H}}\chi_H\right)^{1/2}k^2 P$$
$$= \frac{\left[(g/k)^2\left(\sin^2\Theta - \chi_0\right) + \chi_{\overline{H}}\chi_H P^2\right]^{1/2} - (1/2)(g/k)^2}{\left(\chi_{\overline{H}}\chi_H\right)^{1/2}P}. \quad (19)$$

References

Batterman, B. W. & Cole, H. (1964). *Rev. Mod. Phys.* **36**, 681–717.
Bedzyk, M. J., Bommarito, G. M. & Schildkraut, J. S. (1989). *Phys. Rev. Lett.* **62**, 1376–1379.
Brauer, H. E., Ekvall, I., Olin, H., Starnberg, H. I., Wahlström, E., Hughes, H. P. & Strocov, V. N. (1997). *Phys. Rev. B*, **55**, 10022–10026.
Brennan, S. & Cowan, P. L. (1992). *Rev. Sci. Instrum.* **63**, 850–853.
Brümmer, O., Höche, H. R. & Nieber, J. (1979). *Phys. Status Solidi A*, **53**, 565–570.
Caticha, A. & Caticha-Ellis, S. (1982). *Phys. Rev. B*, **25**, 971–983.
Cowan, P. L., Golovchenko, J. A. & Robbins, M. F. (1980). *Phys. Rev. Lett.* **44**, 1680–1683.
DuMond, J. W. M. (1937). *Phys. Rev.* **52**, 872–883.
Graeff, W. & Materlik, G. (1982). *Nucl. Instrum. Methods*, A**195**, 97–103.
Iida, A., Matsushita, T. & Ishikawa, T. (1985). *Jpn. J. Appl. Phys.* **24**, L675–678.
Larsson, C. U. S., Beutler, A., Björneholm, O., Federman, F., Hahn, U., Rieck, A., Verbin, S. & Möller, T. (1994). *Nucl. Instrum. Methods*, A**337**, 603–608.
Materlik, G., Zegenhagen, J. & Uelhoff, W. (1985). *Phys. Rev. B*, **32**, 5502–5505.
Riekel, C. (1976). *J. Solid State Chem.* **17**, 389–392.
Sugiyama, M., Maeyama, S., Maede, F. & Oshima, M. (1995). *Phys. Rev. B*, **52**, 2678–2681.
Woodruff, D. P., Seymour, D. L., McConville, C. F., Riley, C. E., Crapper, M. D., Prince, N. P. & Jones, R. G. (1987). *Phys. Rev. Lett.* **58**, 1460–1462.
Woodruff, D. P., Seymour, D. L., McConville, C. F., Riley, C. E., Crapper, M. D., Prince, N. P. & Jones, R. G. (1988). *Surf. Sci.* **195**, 237–254.
Wu, Z. Y., Ouvrard, G., Lemaux, S., Moreau, P., Gressier, P., Lemoigno, F. & Rouxel, J. (1996). *Phys. Rev. Lett.* **77**, 2101–2104.
Zegenhagen, J. (1993). *Surf. Sci. Rep.* **18**, 199–271.
Zegenhagen, J., Materlik, G. & Uelhoff, W. (1990). *J. X-ray Sci. Technol.* **2**, 214–239.

 Received 19 July 2000 • Accepted 23 March 2001